Electrical Power and Energy Systems 155 (2024) 109666

Contents lists available at ScienceDirect

International Journal of Electrical Power and Energy Systems

journal homepage: www.elsevier.com/locate/ijepes

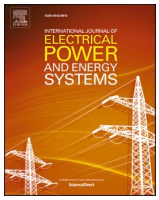

A smith-predictor-assisted adaptive load disturbance rejection controller for speed variation suppression of PMSM drive

Chao Zhang [a,*], Liwei Zhang [a], Dong Wang [b,*], Kaiyuan Lu [b]

[a] School of Electrical Engineering, Beijing Jiaotong University, 100044 Beijing, China
[b] Department of Energy Technology, Aalborg University, 9220 Aalborg, Denmark

ARTICLE INFO

Keywords:
Permanent magnet synchronous machine
Disturbance rejection control
Speed dynamic response
Smith predictor
Adaptive sliding mode disturbance observer

ABSTRACT

The load disturbance rejection ability of the electrical machine systems is an important consideration factor in many applications, including both power generation (e.g., wind power generator) and consumption (e.g., servo systems such as high-precision machining and continuous motion in manufacturing automation). Existing studies on load disturbance rejection mainly focus on developing disturbance observers with improved steady state and dynamic performance. However, the performance of the disturbance rejection control is not only determined by the performance of the disturbance observers but also influenced by the speed response control during the transient. The latter problem might require more attention, especially due to the fact that speed filter is widely used in many actual systems to suppress the speed ripples or noise. The speed control performance would suffer from the delay caused by the filter and result in an undesired oscillatory speed response. In this paper, load disturbance rejection control based on a sliding mode disturbance observer is considered as an investigation platform, where an adaptive filter is proposed to further improve the performance of the observer. More importantly, a Smith predictor-based speed filter delay compensator is proposed to mitigate the undesired variation in the speed response caused by speed filter, achieving enhanced transient speed response under load disturbance. This structure is simple to implement, and no control parameters need to be tuned. The effectiveness of the proposed solution has been verified on a permanent magnet synchronous machine drive system.

1. Introduction

Permanent magnet synchronous machine (PMSM) has found widespread applications in both electrical power generation and consumption fields, such as wind power generator [1,2], electric vehicle drive [3,4], industrial automation [5], and others due to its high efficiency and power density. In many servo drive systems, such as those used in high-precision machining and continuous motion in high-throughput manufacturing automation, the ability to maintain system speed at its reference point is a crucial factor to consider. Specifically, the speed must exhibit low ripple and noise at steady-state conditions while also recovering quickly with minimal fluctuation during transients. The above requirements also apply to power generation applications, such as the stability of the power system relies on maintaining the synchronous operation of interconnected synchronous generators [6]. If the speed/frequency cannot recover quickly and accurately after a disturbance occurs, it will disrupt the frequency balance of the system, impacting power quality and potentially leading to system collapse. Therefore, many methods are proposed for improving the rotor speed/frequency stability. e.g., frequency synchronization control [6], automatic frequency control [7], and an adaptive droop control [8].

According to the above analysis, improving the disturbance rejection and maintaining the speed stability are very important to PMSM for both generating and motoring applications. Existing research activities mainly focus on developing disturbance observers for fast and accurate detection of load disturbance, so that it can be appropriately compensated to reduce its influence on the system speed performance. Various types of observers are adopted to achieve disturbance observation, such as extended state observer [9], Kalman filter [10], reduced-order observer [11], Internal model observer [12], Luenberger observer [13], sliding mode observer based on the integral terminal sliding surface [14] and sliding mode observer based on an additional feedback loop [15]. In [9] and [10], the response time of the observer against a step change is around 0.02 s, while in [11] it is 0.1 s, and in [15] it is about 0.2 s. It can be observed that regardless of which type of observer structure is used, the disturbance detection and compensation always

* Corresponding authors.
E-mail addresses: sakura_sci@163.com (C. Zhang), dwa@energy.aau.dk (D. Wang).

https://doi.org/10.1016/j.ijepes.2023.109666
Received 15 March 2023; Received in revised form 31 July 2023; Accepted 15 November 2023
Available online 24 November 2023

lag behind the actual disturbance's effect. Speed transient is inevitable even with disturbance rejection control. Therefore, it is also very important to perform fast and reliable speed control to achieve high-performance servo system against load disturbance. This issue may need more attention, especially considering that speed filters are widely used in many actual systems to suppress speed ripples or noise, at the cost of degraded speed performance during transients. Measurement noise is typically unavoidable in modern drive systems. For example, the compact drive design may lead to electromagnetic interference (EMI) problems, which become severe when the DSP control board and power module are not fully isolated. Furthermore, the quantization error in the discrete-time controller also results in measurement noise [16,17]. To suppress the noise, various types of speed filters are adopted, i.e., phase-locked loop speed filter [18], speed filter based on proportional-integral-resonant [19], and resonant-based speed ripple mitigation method [17]. However, the delay caused by the filter will result in degraded speed performance during transients [20]. The degradation in speed control is normally acceptable in many industrial applications. However, for those servo applications with high requirements for speed control, the influence of the speed filter regarding the system load disturbance rejection ability, to the best of the authors' knowledge, has not been addressed in the scientific literature. Thus, load disturbance rejection control with the assistance of speed filter delay compensation is studied in this paper.

This paper adopts the sliding mode disturbance observer (SMDO) as the load disturbance observer due to its excellent robustness to uncertainties and disturbance performance. The SMDO proposed in [21] has proven that the effect is equivalent to the output of filtering real system disturbance. This kind of low-pass filter (LPF) is called virtual LPF [22]. The chattering can be arbitrarily suppressed by tuning the cut-off frequency of the virtual LPF [23], but the dynamic response will also be reduced [24]. For fast disturbance detection, the virtual LPF should have a high cut-off frequency, which requires the SMDO gain to be aggressive. However, noisy speed information fed into the SMDO can introduce noise in the observed disturbance, resulting in a more severe chattering problem if the SMDO is designed too aggressively [25]. To mitigate the above problem, an adaptive filter structure is introduced into the conventional SMDO, in order to obtain smooth quasi-steady-state output when the disturbance varies slowly and fast dynamic response during the fast transient such as step change. More importantly, with the aim of enhancing the load disturbance rejection performance, this paper proposes an advanced disturbance rejection controller by incorporating a Smith predictor structure to compensate for the filter delay, so that the deterioration of speed control performance during transient can be resolved. The Smith predictor was proposed by J. M. Smith [26], and it has been applied in many fields, such as power systems, in which, it is usually used to compensate for signal transmission time delay [27] and reduce the impact of communication delays [28]. Nowadays, the Smith predictor has been adopted in the discrete-time current controller of electrical machine drives to compensate for fixed time delay caused by inherent system dead time [29], calculation [30], and signal transmission [31]. However, how to solve the speed filter delay problem by using a Smith predictor, to the best of the author's knowledge, has not been appropriately addressed in the scientific literature. Experimental results in this paper demonstrate that the proposed solution, which uses a Smith predictor to enhance speed response during transients, offers improved disturbance rejection ability.

The rest of the paper is organized as follows: In section II, an adaptive SMDO is introduced for achieving fast observation as well as smooth steady-state output. Based on the experimental results, the speed control deterioration caused by the speed filter is pointed out to be the main challenge to be solved. In section III, the influence of the speed filter during the transient is analyzed and a compensation structure based on the Smith predictor is proposed to solve the speed deterioration during the transient. Besides, the stability and parameter robustness analysis of the proposed method are included in this section as well. Experiments results are given for validation in section IV. Finally, section V concludes this paper.

2. The adaptive sliding mode disturbance observer

The conventional SMDO incorporated with an adaptive LPF (ALPF) for achieving both smooth output at steady states and fast response during transients is presented in this section. A performance comparison with super-twisting SMDO (STSMDO) shows that the proposed adaptive SMDO (ASMDO), which is a combination of ALPF and conventional SMDO, demonstrates improved steady-state performance at both no-load and loaded conditions, while good dynamic performance during transients is preserved. Thus, ASMDO is chosen as the disturbance rejection platform, where the speed filter delay compensation is further investigated based on this platform.

2.1. Mathematic model of PMSM

The mechanical equation of PMSM is shown as

$$J\frac{\mathrm{d}\omega_\mathrm{m}}{\mathrm{d}t} = K_\mathrm{T} i_\mathrm{q} - B\omega_\mathrm{m} - T_\mathrm{L} \tag{1}$$

where J is the moment of the inertia; B is the viscosity coefficient; K_T is the torque constant; i_q is the q-axis current; T_L is the load torque; ω_m is the mechanical angular velocity.

When designing the disturbance observer, the concept of total disturbance is introduced, where parameter uncertainties and the uncertain disturbance are involved [35,37]. Then, (1) can be described as

$$\begin{cases} \dfrac{\mathrm{d}\omega_\mathrm{m}}{\mathrm{d}t} = \dfrac{K_{\mathrm{T}0}}{J_0} i_\mathrm{q} - \dfrac{d}{J_0} \\ d = (B_0 + \Delta B)\omega_\mathrm{m} + T_\mathrm{L} + T_\mathrm{d} + \Delta J\dot{\omega}_\mathrm{m} - \Delta K_\mathrm{T} i_\mathrm{q} \end{cases} \tag{2}$$

where J_0, B_0, and $K_{\mathrm{T}0}$ are the actual moment of the inertia, actual viscosity coefficient, and actual torque constant respectively; ΔJ, ΔB, and ΔK_T are the parameter uncertainties; T_d is the uncertain disturbance; d is the total disturbance.

2.2. The conventional sliding mode disturbance observer

Many different types of SMDOs can be connected in series with ALPF to form an adaptive SMDO. Thus, any type of SMDO can be used. In this paper, the proposed observer in [32] is used as an example. The principle is reviewed as follows.

The sliding mode surface s is defined as

$$s = \widehat{\omega}_\mathrm{m} - \omega_\mathrm{m} \tag{3}$$

where $\widehat{\omega}_\mathrm{m}$ is the estimated mechanical angular velocity.

The sliding mode disturbance observer is designed as

$$\frac{\mathrm{d}\widehat{\omega}_\mathrm{m}}{\mathrm{d}t} = \frac{K_{\mathrm{T}0}}{J_0} i_\mathrm{q} - \frac{k_\mathrm{smo}}{J_0}\mathrm{sign}(s) \tag{4}$$

where k_smo is the observer gain. Sign(s) is the symbolic function.

Subtract (2) from (4) to get

$$\frac{\mathrm{d}s}{\mathrm{d}t} = \frac{d}{J_0} - \frac{k_\mathrm{smo}}{J_0}\mathrm{sign}(s) \tag{5}$$

When the observer enters the equilibrium state, the following equations will be satisfied

$$\begin{cases} s = 0 \\ \dfrac{\mathrm{d}s}{\mathrm{d}t} = 0 \end{cases} \tag{6}$$

At this time, the total disturbance d can be expressed as

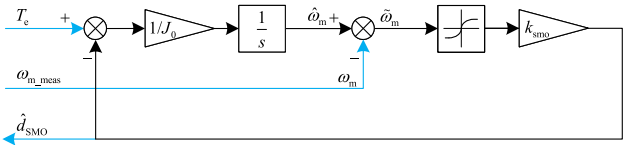

Fig. 1. The block diagram of sliding mode disturbance observer.

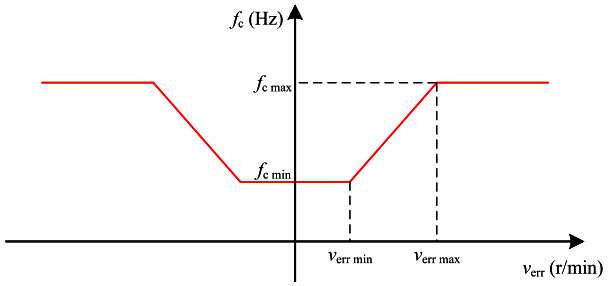

Fig. 2. The relationship between cut-off frequency and speed error.

$$d = k_{smo}\text{sign}(s) \tag{7}$$

Because reference [33,34], and [35] prove that the chattering can be suppressed by using the hyperbolic tangent function. Therefore, in this paper, the symbolic function is replaced by the hyperbolic tangent function for improving the SMDO performance and (7) is changed as

$$\begin{cases} d = k_{smo}\tanh(s) \\ \tanh(s) = \dfrac{e^{ms} - e^{-ms}}{e^{ms} + e^{-ms}} \end{cases} \tag{8}$$

where m is the hyperbolic tangent function gain.

According to the literature [32], the stable condition can be expressed as

$$k_{smo} > |d| \tag{9}$$

The block diagram of sliding mode disturbance observer is shown in Fig. 1.

2.3. Adaptive low pass filter

Although the hyperbolic tangent function can suppress chattering, it will not eliminate chattering. That means the chattering will be worse with transient performance getting better by increasing the sliding mode gain (k_{smo}). The balance between the dynamic and steady state is still to be solved. This problem is not only in the SMDO used in this paper but also in other types of SMDOs. For solving this kind of problem, in this paper, an ALPF is proposed to balance the dynamic and steady-state performance of the observer. It should be noted that the sliding mode gain needs to be a large value for ensuring a fast enough dynamic performance when using ALPF.

Table 1
Parameters of the experimental system.

Variables	Value	Variables	Value
Proportional gain for speed PI k_p	0.2	Parameter of ALPF $f_{c\,min}$	10 Hz
Integral gain for speed PI k_i	2	Parameter of ALPF $f_{c\,max}$	1500 Hz
Proportional gain for current PI (both in d and q axis) $k_{p\text{-}dq}$	10.6	Parameter of ALPF $v_{err\,min}$	5 r/min
Integral gain for current PI (both in d and q axis) $k_{i\text{-}dq}$	1921	Parameter of ALPF $v_{err\,max}$	30 r/min
Cut-off frequency of speed LPF f_{sL}	15 Hz	Observer gain k_{smo}	1000
Cut-off frequency of inner loop ω_c	2094 rad/s	hyperbolic tangent function gain m	0.01
Moment of inertia J_0	12.7×10^{-3} kg·m^2		

The input (x) and output (y) of a traditional LPF can express as

$$\frac{y}{x} = \frac{2\pi f_c}{s + 2\pi f_c} \tag{10}$$

where f_c is the cut-off frequency and is a fixed constant for traditional LPF.

In ALPF, the cut-off frequency is determined by speed error. The specific relationship is shown in Fig. 2.

In Fig. 2, there are four parameters ($f_{c\,min}$, $f_{c\,max}$, $v_{err\,min}$, and $v_{err\,max}$) needed to be selected when ALPF is used. When selecting the values of these parameters, the following principles can be referred to.

1. The value of $f_{c\,min}$ should be chosen appropriately small to filter out steady-state ripples caused by chattering or speed measurement noise when the ALPF has a constant cut-off frequency of $f_{c\,min}$.
2. The value of $f_{c\,max}$ should be sufficiently large to ensure a satisfactory dynamic response of the disturbance observation when the ALPF has a constant cut-off frequency equal to $f_{c\,max}$.
3. The value of $v_{err\,min}$ should be slightly (e.g., 2 ~ 3 times) larger than the speed ripple in the steady state.
4. The value of $v_{err\,max}$ should be sufficiently (e.g., 5 ~ 6 times) larger than $v_{err\,min}$.

2.4. Experimental results

To demonstrate that the proposed adaptive filter can improve the performance of the conventional SMDO. LPFs with fixed and adaptive cut-off frequencies are incorporated into the control system respectively.

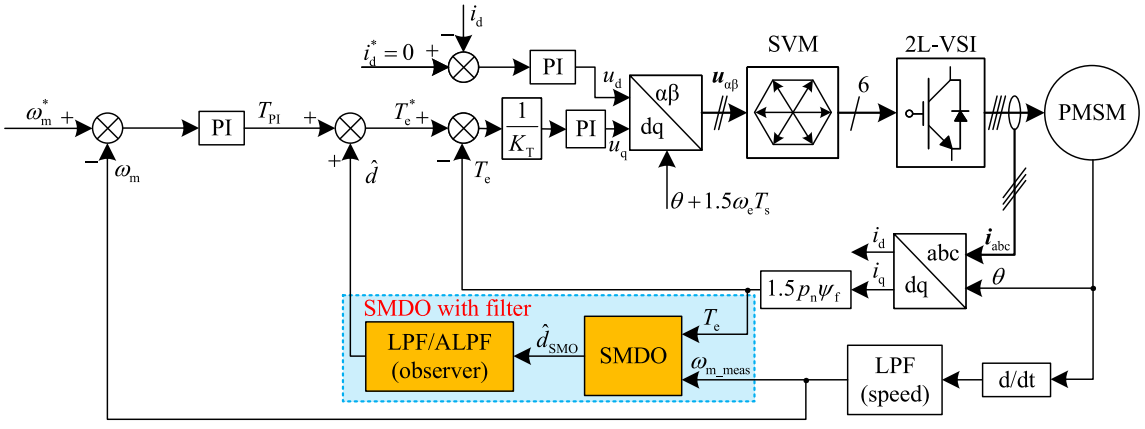

Fig. 3. The system block diagram with a sliding mode disturbance observer.

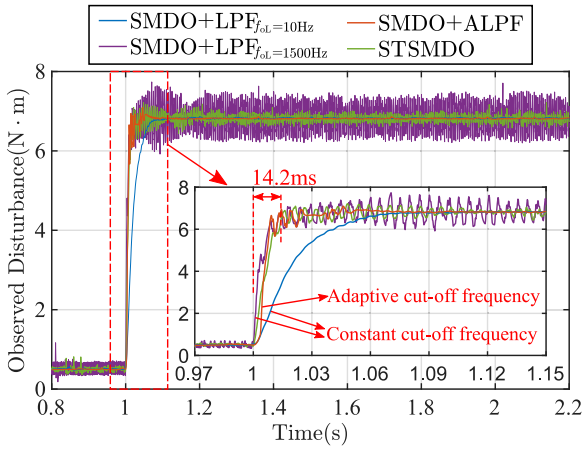

Fig. 4. The experimental-observed disturbance results for different methods. (Step disturbance occurs at 1 s).

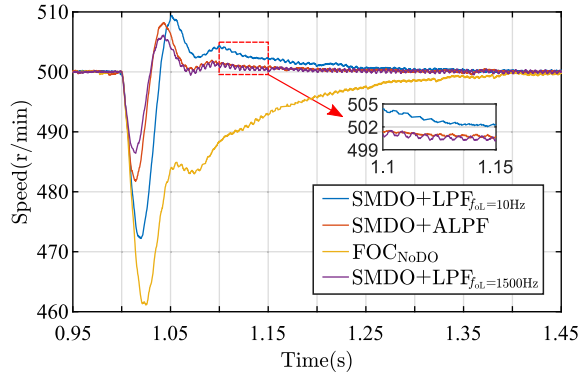

Fig. 5. The experimental speed responses of the four different working conditions. 1. SMDO + LPF (constant cut-off frequency is 10 Hz). 2. SMDO + LPF (constant cut-off frequency is 1500 Hz). 3. SMDO + ALPF (cut-off frequency changes with speed error). 4. FOC without any disturbance observer. Step disturbance occurs at 1 s. NoDO means No Disturbance Observer.).

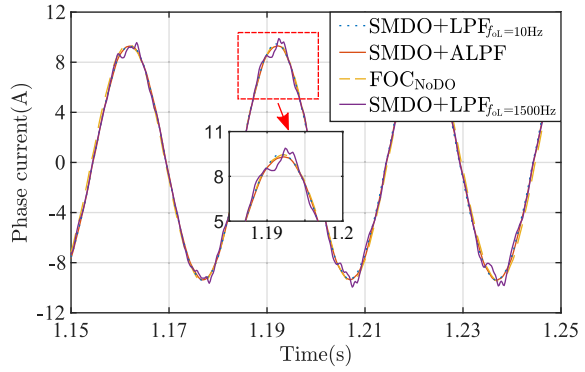

Fig. 6. The experimental phase current comparison results with four different working conditions. (NoDO means No Disturbance Observer.).

The block diagram and the parameters of the control system are shown in Fig. 3 and Table 1 respectively. It should be noticed in Fig. 3 that a speed LPF is added to smoothen the speed feedback in the speed control loop.

In Table 1, the parameters of speed and current PI controller are calculated according to the selection principle based on bandwidth in [36], and the calculated values are fine-tuned in the experiment as the final values. The parameters of SMDO are determined by parameter sweeping according to the dynamic performance requirements. The parameters of ALPF are selected according to the principles described in section 2.3.

The experimental results comparison of observed disturbance, measured speed, and phase current are shown in Fig. 4, Fig. 5, and Fig. 6, respectively. The four working conditions are,

1. SMDO + LPF. The constant cut-off frequency is 10 Hz. The experimental results are represented by the blue curve.
2. SMDO + LPF. The constant cut-off frequency is 1500 Hz. The experimental results are represented by the purple curve.
3. SMDO + ALPF. The adaptive cut-off frequency changes with the speed error (parameters are listed in Table 1). The experimental results are represented by the dark red curve.
4. FOC (field-oriented control) without any disturbance observer and observer filter. The experimental results are represented by the yellow curve.

For working condition (3) (SMDO + ALPF). When a step disturbance occurs, the absolute value of speed error will increase immediately. During this process, according to Fig. 2, the adaptive cut-off frequency will increase from $f_{c\ min}$(10 Hz) to $f_{c\ max}$(1500 Hz). When the adaptive cut-off frequency is about 1500 Hz, the observed disturbance from ALPF (dark red curve) becomes similar to that from working condition (2) (purple curve).

When the speed prepares to return to the steady state, the absolute value of speed error will gradually decrease to zero. At this time, according to Fig. 2, the cut-off frequency of ALPF will decrease from $f_{c\ max}$(1500 Hz) to $f_{c\ min}$(10 Hz). Therefore, the speed measurement noise is eliminated gradually in this process, and a similar observed result from working condition (1) (blue curve) is obtained, as shown in the results between 1.09 s and 1.15 s in the zoomed-in diagram in Fig. 4.

To show the good observation performance of ASMDO (ALPF + SMDO), the super-twisting sliding mode disturbance observer (STSMDO) reported in [37] and [38] is tested in the experimental platform and the symbolic function in STSMDO is also replaced by the hyperbolic tangent function for a fair comparison. The experimental result (depicted by the green curve in Fig. 4) indicates that the STSMDO exhibit similar transient response to ASMDO. However, the steady-state ripple of ASMDO is much smaller than that of STSMDO at loaded condition. Considering the good steady-state performance and comparable dynamic response, ASMDO is chosen as the disturbance rejection platform for further investigation.

The observed disturbance will feed forward to the torque (current) control loop as part of the torque (current) command, which reduces the speed settling time. It will spend less time for the measured speed to return to the steady state compared with the conventional FOC (without the disturbance observer and the observer filter). This analysis is consistent with the experimental results shown in Fig. 5.

Fig. 5 indicates the disturbance observer can improve the transient performance. Meanwhile, the faster the disturbance is observed, the less effect the speed is affected by the disturbance. Although under working condition (2) (purple curve. the observer filter has a constant cut-off frequency of 1500 Hz), the speed response is the best, the observed disturbance ripple in steady state is also the largest (shown in 1.09 s ~ 1.15 s of Fig. 4). It can also be observed in Fig. 5 that the measured speed with 1500 Hz cut-off frequency LPF has largest ripples (e.g., during 1.10 s ~ 1.15 s). Moreover, the phase currents are measured and compared when different LPFs are implemented in disturbance observation. It can be seen in Fig. 6 that the load disturbance compensation with larger ripple causes the phase current to be distorted. i.e., the working condition (2) (purple curve), f_{oL} = 1500 Hz, has an obvious phase current distortion.

Moreover, it should be pointed out that even the speed response has been improved by introducing the disturbance observation and compensation as shown in Fig. 5, the performance is still not very satisfactory due to the undesirable speed overshoot/variation. This phenomenon might be due to the delay caused by the speed filter as discussed in the following section. Therefore, it is worthwhile to investigate this problem further.

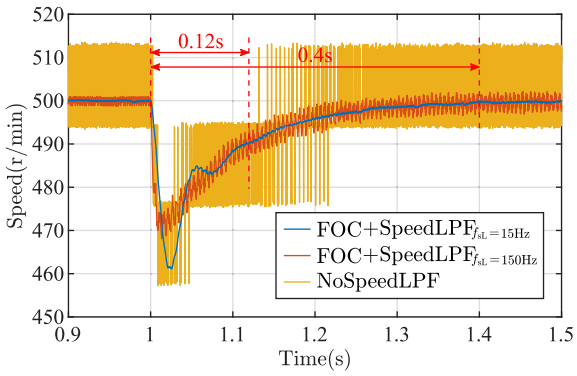

Fig. 7. The experimental speed waveforms with and without a speed LPF.

3. Smith predictor-based speed filter delay compensation

The speed measurement noise from the quantization error or EMI will negatively influence the system performance [16] and a speed filter (e.g., a traditional LPF) is often adopted to reject the noise. However, the filter will introduce time delay between the measured and the actual speed signal during speed transient [20,39] resulting deteriorated speed response, such as oscillation. This conclusion is well proved by the experimental results shown in Fig. 7. The yellow waveform indicates that the measured speed signal without using a filter includes lots of noise caused by quantization error. The rest of the waveforms show that using a speed filter can well eliminate the noise. But the speed oscillation/variation caused by speed filter delay becomes more obvious as the cut-off frequency of the filter decreases.

For traditional FOC, the oscillatory speed caused by filter delay will be acceptable in many industrial applications. However, for those servo applications, the oscillatory speed will significantly impact the system performance after adding a high-performance disturbance observer, like the results in Fig. 5, where undesired speed overshoot/variation can be observed. The specific reason and solution will explain in detail in this section.

3.1. Analysis of the speed oscillation during transient

In Fig. 8, k_p and k_i are the proportional and integral gains of the speed PI controller. The torque (current) inner loop is seen as a first-order system [36], ω_c and $C(s)$ are the cut-off frequency and the transfer function of the torque (current) inner loop respectively. J_0 is the moment of inertia. f_{sL} is the cut-off frequency of speed LPF, and $\omega_{sL} = 2\pi f_{sL}$. d and $\hat{d}$ are the actual and estimated total disturbance respectively.

According to Fig. 8 (a), the transfer function without the speed LPF can be expressed as

$$\begin{aligned}\omega_m &= \frac{G_{PI}CG}{1+G_{PI}CG}\omega_{ref} + \frac{-G}{1+G_{PI}CG}d + \frac{CG}{1+G_{PI}CG}\hat{d} \\ &= g_{11}\omega_{ref} + g_{12}d + g_{13}\hat{d}\end{aligned} \tag{11}$$

According to Fig. 8 (b), the transfer function with the speed LPF can be expressed as

$$\begin{aligned}\omega_m &= \frac{G_{PI}CGG_{LPF}}{1+G_{PI}CGG_{LPF}}\omega_{ref} + \frac{-GG_{LPF}}{1+G_{PI}CGG_{LPF}}d + \frac{CGG_{LPF}}{1+G_{PI}CGG_{LPF}}\hat{d} \\ &= g_{21}\omega_{ref} + g_{22}d + g_{23}\hat{d}\end{aligned} \tag{12}$$

The expressions of g_{11}, g_{12}, g_{13}, g_{21}, g_{22}, and g_{23} in (11) and (12) are

$$\begin{cases} g_{11} = \dfrac{k_p\omega_c s + k_i\omega_c}{A_1} \\ g_{12} = \dfrac{-s^2 - \omega_c s}{A_1} \\ g_{13} = \dfrac{\omega_c s}{A_1} \\ A_1 = J_0 s^3 + J_0\omega_c s^2 + k_p\omega_c s + k_i\omega_c \end{cases} \tag{13}$$

$$\begin{cases} g_{21} = \dfrac{k_p\omega_c\omega_{sL}s + k_i\omega_c\omega_{sL}}{A_2} \\ g_{22} = \dfrac{-\omega_{sL}s^2 - \omega_c\omega_{sL}s}{A_2} \\ g_{23} = \dfrac{\omega_c\omega_{sL}s}{A_2} \\ A_2 = J_0 s^4 + J_0(\omega_c+\omega_{sL})s^3 + J_0\omega_c\omega_{sL}s^2 + k_p\omega_c\omega_{sL}s + k_i\omega_c\omega_{sL} \end{cases} \tag{14}$$

The transfer functions in (13) and (14) are high-order, and it is difficult to obtain the analytical expressions of the closed-loop poles. Therefore, the poles are calculated numerically by inserting the values of the system parameters (listed in Table 1) into the equations. The

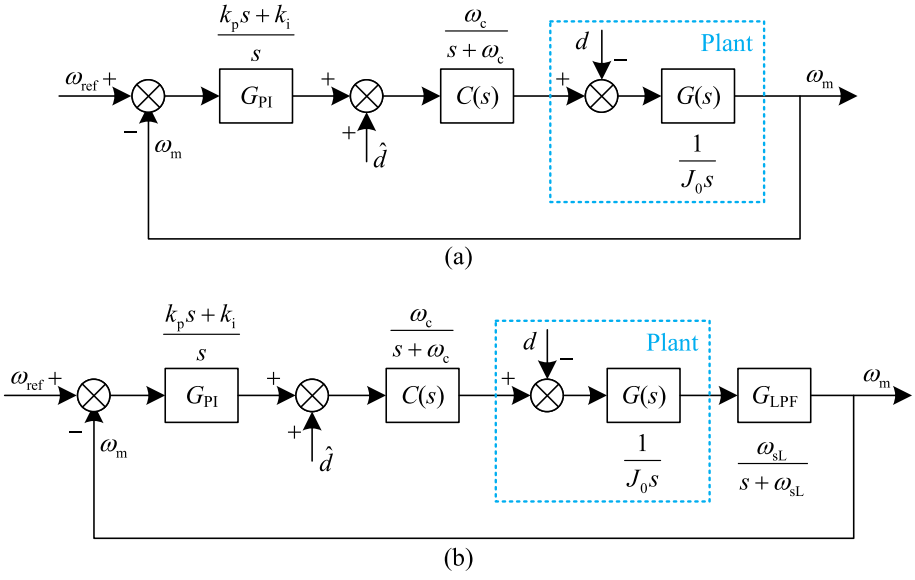

Fig. 8. The structure diagram of the control system. (a) without a speed LPF. (b) with a speed LPF.

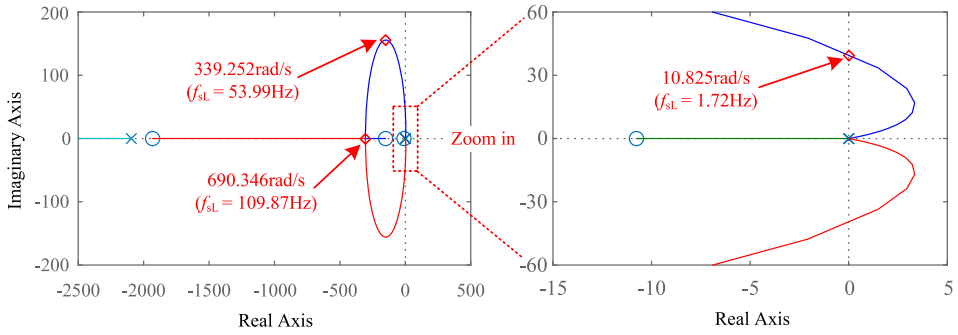

Fig. 9. The closed-loop root locus of the control systems with speed LPF. ('o' and 'x' represent the equivalent open-loop zeros and poles, respectively, of the system with speed filter and the right figure is the zoomed show of the indicated part in the left figure.).

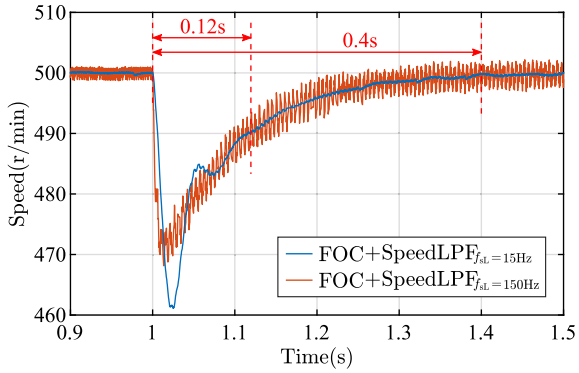

Fig. 10. The experimental speed responses using a traditional LPF (the speed LPF has a fixed cut-off frequency).

parameter ω_c in Table 1 is obtained in Matlab/system identification toolbox by using the experimental data of the inner loop response.

According to the calculation results, the system without speed LPF has three closed-loop poles, and they are −1931.8, −151.4, and −10.8. Therefore, the system is stable and exhibits exponential decay. However, this situation will change after introducing a speed LPF.

To show the effect of speed LPF in detail, the cut-off frequency $\omega_{sL}(2\pi f_{sL})$ of the speed filter is used as the variable parameter, and the closed-loop root locus is shown in Fig. 9, where the right figure provides a zoomed-in view of the indicated part (rectangular region with red dotted boundary) in the left figure.

As Fig. 9 indicates, after introducing the speed LPF, the closed-loop poles change as the cut-off frequency f_{sL} changes. i.e., when $f_{sL} <$ 1.72 Hz, the poles located on the right side of the imaginary axis make the system unstable. When 1.72 Hz $< f_{sL} <$ 109.87 Hz, there will be two poles on the negative real axis and a pair of conjugate poles located on the left half-plane. The conjugate poles indicate that are oscillating response can be observed, which matches very well with the measured speed response shown in Fig. 10 when $f_{sL} = 15$ Hz. As the f_{sL} increase, when $f_{sL} > 110$ Hz the conjugate poles will move to the negative real axis, indicating that there will be no oscillation in the speed response, as shown in Fig. 10 when $f_{sL} = 150$ Hz. But the high cut-off frequency results in more pronounced speed ripple because less speed measurement noise is filtered out.

As Fig. 10 shows, in traditional FOC, the speed transient time (about 0.4 s) is longer than the oscillation time (the speed oscillation becomes unobvious after 0.12 s). The oscillation is a secondary factor in the transient, then the small cut-off frequency can be chosen. However, with the introduction of an improved disturbance observer, the oscillation becomes the main influencing factor during transient (as the speed overshoot phenomenon in Fig. 5 shows). To eliminate the oscillation, the cut-off frequency needs to be increased, but it will destroy the speed measurement noise suppression performance in the steady state (as the results in Fig. 10 show).

Therefore, it is necessary to propose a method to compensate the speed filter delay.

3.2. The basic principle of Smith predictor

In terms of (11) and (12), after adding the speed LPF, the G_{LPF} in the denominator causes the conjugate poles. If the G_{LPF} in the denominator can be removed, the undesired speed overshoot/variation problem in Fig. 5 may be mitigated. For serving this purpose, a speed filter delay compensation structure based on Smith predictor is proposed.

The basis of the Smith predictor is to add a structure shown in Fig. 11 to the control system. $\hat{G}(s)$ is the estimated transfer function of the PMSM. The LPF in the Smith predictor is the same as the speed LPF.

After adding the Smith predictor, the system transfer function can be expressed as

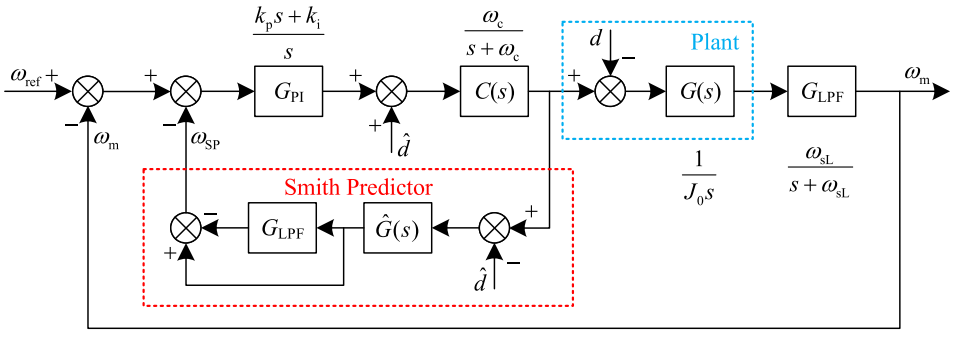

Fig. 11. The system block diagram with the proposed Smith predictor compensation scheme.

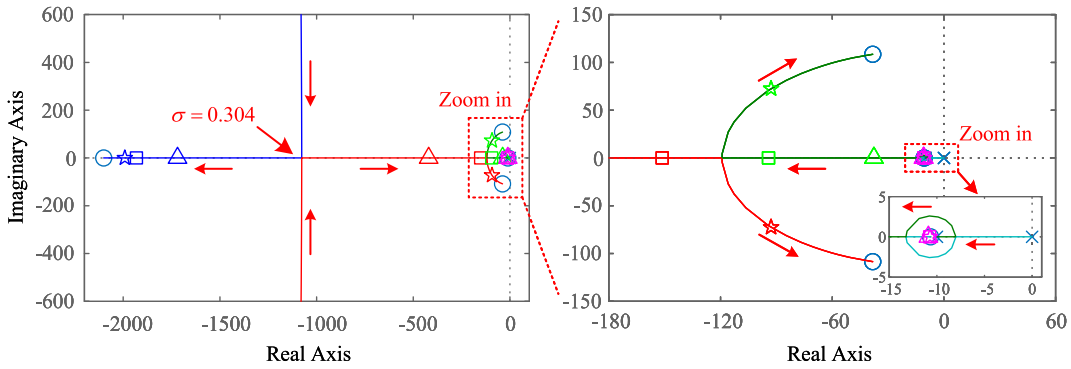

Fig. 12. The closed-loop root locus of the drive systems with the moment of inertia mismatch. ("△", "□", and "☆" represent the roots when σ is equal to 0.5, 1, and 1.5 respectively.).

$$\begin{aligned}\omega_m &= \frac{G_{PI}CGG_{LPF}}{1+G_{PI}CGG_{LPF}+G_{PI}C\widehat{G}(1-G_{LPF})}\omega_{ref} \\ &+\frac{-GG_{LPF}[1+G_{PI}C\widehat{G}(1-G_{LPF})]}{1+G_{PI}CGG_{LPF}+G_{PI}C\widehat{G}(1-G_{LPF})}d \\ &+\frac{CGG_{LPF}[1+G_{PI}\widehat{G}(1-G_{LPF})]}{1+G_{PI}CGG_{LPF}+G_{PI}C\widehat{G}(1-G_{LPF})}\widehat{d} \\ &= g_{31}\omega_{ref}+g_{32}d+g_{33}\widehat{d}\end{aligned} \tag{15}$$

where,

$$\begin{cases} g_{31} = \dfrac{k_p\omega_c\omega_{sL}s+k_i\omega_c\omega_{sL}}{A_1(s+\omega_{sL})} \\ g_{32} = \dfrac{-J_0\omega_{sL}s^3-J_0(\omega_c\omega_{sL}+\omega_{sL}^2)s^2-(k_p\omega_c\omega_{sL}+J_0\omega_c\omega_{sL}^2)s-k_i\omega_c\omega_{sL}}{J_0A_1(s+\omega_{sL})^2} \\ g_{33} = \dfrac{J_0\omega_c\omega_{sL}s^2+(k_p\omega_c\omega_{sL}+J_0\omega_c\omega_{sL}^2)s+k_i\omega_c\omega_{sL}}{J_0A_1(s+\omega_{sL})^2} \end{cases} \tag{16}$$

As can be observed from (13) and (16), the newly introduced Smith predictor will add a double-pole -ω_{sL} compared to the system (Fig. 8 (a)) without the speed filter and Smith predictor, which is described by (13). The conjugate poles introduced by the speed filter disappear. Moreover, compared with existing poles (-1931.8, −151.4, and −10.8), the newly added double pole -ω_{sL} (-$2\pi \times 15 \approx -94.25$ rad/s) is a bit far away from the dominant pole (-10.8) of the system described in (13), i.e., FOC + ASMDO without the speed LPF. Thus, the speed response of the proposed control scheme, i.e., with SP-structure to compensate the error caused by the speed LPF, would have similar dynamic performance (but with much less noise/ripples) compared to the system without the speed LPF, which means the undesired speed overshoot/variation problem is solved effectively.

3.3. Stability analysis

As mentioned above, the system without speed filter shown in Fig. 8 (a) has three closed-loop poles (−1931.8, −151.4, and −10.8), which are negative and indicate that the system is stable.

After introducing a speed LPF to smooth the speed signal, the original third-order system transforms into a fourth-order system, and the corresponding root locus is shown in Fig. 9. The root locus indicates that the system is stable when the cut-off frequency f_{sL} of the speed LPF exceeds 1.72 Hz. Considering that the cut-off frequency of 15 Hz effectively smoothens the speed curve, it is selected as the value for f_{sL}. However, this will result in a pair of conjugate poles -38.3 ± 108.5i, resulting in undesired speed oscillation/variation during transient. Thus, a Smith predictor-based delay compensation scheme is proposed to mitigate this problem.

When the SP structure is introduced to the control scheme, the transfer function is shown in (15) and (16). The closed-loop characteristic equation under disturbance becomes

$$J_0A_1(s+\omega_{sL})^2 = J_0(s+1931.8)(s+151.4)(s+10.8)(s+2\pi\times 15)^2 = 0 \tag{17}$$

Since all five roots are negative and lie on the left half-plane, the proposed solution is stable. Moreover, as discussed in section 3.2, the undesired speed overshoot/variation problem is solved as well.

3.4. The robustness of parameter mismatch

According to the system block diagram given in Fig. 11, the moment

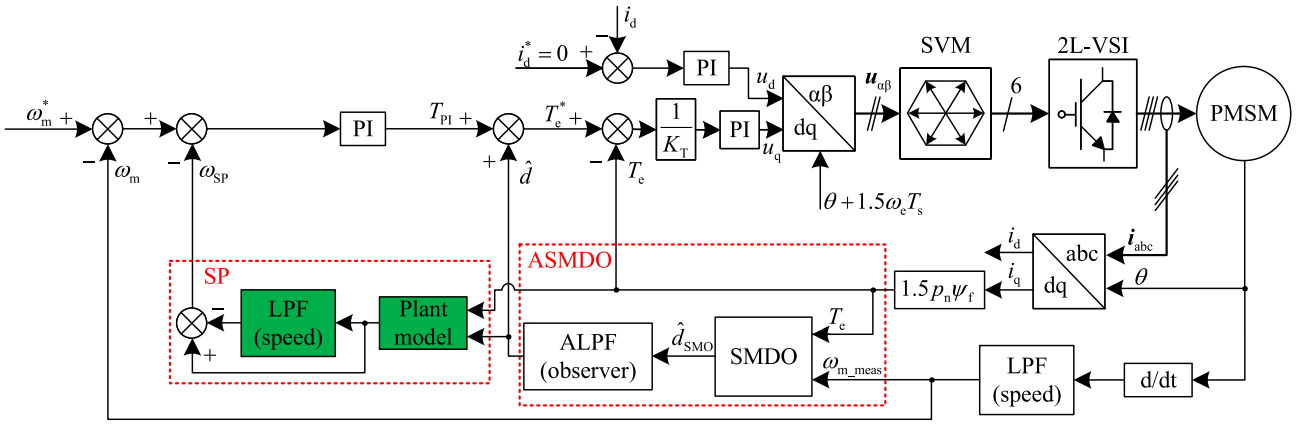

Fig. 13. The system block diagram of FOC + ASMDO + SP.

of inertia is the only motor parameter involved. Therefore, the robustness against the moment of inertia variation will be analyzed.

When analyzing (15), it is assumed that the $\widehat{G}(s)$ is equal to the plant model $G(s)$. This implies that the moment of inertia in the controller is the same as the one in the plant model. However, there will always be a deviation between the used value of the moment of inertia and its actual value. Therefore, it is necessary to analyze the stability of the proposed Smith-predictor-assisted adaptive load disturbance rejection controller and assess its capability to effectively handle the time delay of the speed LPF.

To analyze the influence of parameter mismatch, the moment of inertia used in the controller is denoted as $\widehat{J}$. Thus, the plant model used in SP can be expressed as,

$$\widehat{G}(s) = \frac{1}{\widehat{J}s} = \frac{1}{\sigma J_0 s} \tag{18}$$

where σ is the inertia error coefficient; J_0 is the actual value of the moment of inertia.

Substitute (18) into (15) and simplify g_{31}, g_{32} and g_{33} to obtain $\widehat{g}_{31}$, $\widehat{g}_{32}$ and $\widehat{g}_{33}$.

$$\begin{cases} \widehat{g}_{31} = \dfrac{\sigma k_p \omega_c \omega_{sL} s + \sigma k_i \omega_c \omega_{sL}}{D_1(s)} \\ \widehat{g}_{32} = \dfrac{-\sigma J_0 \omega_{sL} s^3 - (\sigma J_0 \omega_{sL}^2 + \sigma J_0 \omega_c \omega_{sL}) s^2 - (\sigma J_0 \omega_c \omega_{sL}^2 + k_p \omega_c \omega_{sL}) s - k_i \omega_c \omega_{sL}}{J_0 (s + \omega_{sL}) D_1(s)} \\ \widehat{g}_{33} = \dfrac{\sigma J_0 \omega_c \omega_{sL} s^2 + (\sigma J_0 \omega_c \omega_{sL}^2 + k_p \omega_c \omega_{sL}) s + k_i \omega_c \omega_{sL}}{J_0 (s + \omega_{sL}) D_1(s)} \\ D_1(s) = \sigma J_0 s^4 + \sigma J_0 (\omega_c + \omega_{sL}) s^3 + (k_p \omega_c + \sigma J_0 \omega_c \omega_{sL}) s^2 + (k_i \omega_c + \sigma k_p \omega_c \omega_{sL}) s + \sigma k_i \omega_c \omega_{sL} \end{cases} \tag{19}$$

According to the above equation, the closed-loop characteristic equation of the system under disturbance is $J_0(s + \omega_{sL})D_1(s) = 0$. One of the characteristic roots is $-\omega_{sL}$ and the remaining roots can be obtained by solving $D_1(s) = 0$. However, it is difficult to obtain the analytical expressions of the roots of this fourth-order equation. In order to analyze the relationship between the characteristic roots and the inertia error coefficient σ, define $D_1(s) = 0$ as a closed-loop characteristic equation of an equivalent unity negative feedback system and choose σ as the gain for the root locus analysis. By separating σ, the equivalent open-loop transfer function of the closed-loop characteristic equation ($D_1(s) = 0$) can be expressed as (20). The parameters used in (20) are shown in Table 1.

$$\begin{cases} D_1(s) = 1 + G_{\text{open - loop}}(s) = 0 \\ \Downarrow \\ G_{\text{open - loop}}(s) = \dfrac{\sigma[J_0 s^4 + J_0(\omega_c + \omega_{sL}) s^3 + J_0 \omega_c \omega_{sL} s^2 + k_p \omega_c \omega_{sL} s + k_i \omega_c \omega_{sL}]}{\omega_c s (k_p s + k_i)} \end{cases} \tag{20}$$

According to the equivalent open-loop transfer function, we can draw the root locus of the closed-loop characteristic equation, i.e., the other four roots of the closed-loop characteristic equation ($J_0(s + \omega_{sL})$ $D_1(s) = 0$). The result is shown in Fig. 12. The right figure is the zoomed-in plot of the root locus near origin and "△", "□", and "☆" represent the roots when σ equals 0.5, 1, and 1.5 respectively.

The results show that the characteristic equation ($D_1(s) = 0$) has 4 roots, two of which (depicted by the green and cyan curves) are close to the origin and exhibit a general tendency to move towards left as σ increases. The other two roots (represented by blue and red curves), which

Table 2
Parameters of the PMSM.

Variables	Value
Stator resistance R_s	1.25 Ω
Stator inductance L_s	6.4 mH
PM flux linkage Ψ_f	0.1213 Wb
Pole pairs p_n	4
Rated speed n	4500 r/min
Rated torque T_{rated}	6 N·m
Rated power	2.7 kW

are located at infinity when $\sigma = 0$, gradually move towards the negative real axis as σ increases, and subsequently move towards the left and right sides respectively after merging. For some extreme situations (i.e., $\sigma =$ 1.5), two roots would become conjugate poles (the corresponding experimental results in Fig. 19 show that although the speed during load transient has an oscillation tendency, the influence is not much).

The root locus and the root $-\omega_{sL}$ ($-2\pi \times 15 \approx -94.2$ rad/s) indicate that the five roots of the closed-loop characteristic equation ($J_0(s + \omega_{sL})$ $D_1(s) = 0$) all lie on the left half-plane. This means the system remains stable even in the presence of moment of inertia mismatch. However, the performance of the speed response during transients could be influenced as illustrated in the below experimental results in section 4.3.

3.5. System overview of the proposed solution

Fig. 13 illustrates the system block diagram of the proposed Smith-predictor-assisted adaptive load disturbance rejection controller. ASMDO is chosen to observe the external disturbance. The estimated disturbance is compensated to the output of the speed controller for disturbance rejection. SP-based delay compensator, which requires

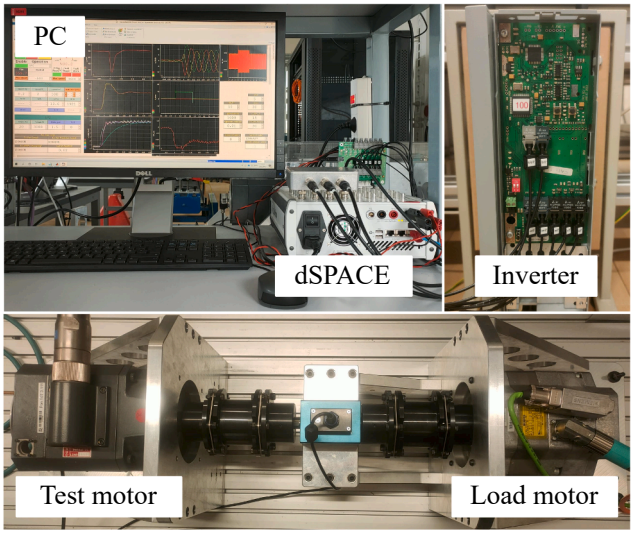

Fig. 14. Experimental platform of PMSM drive system.

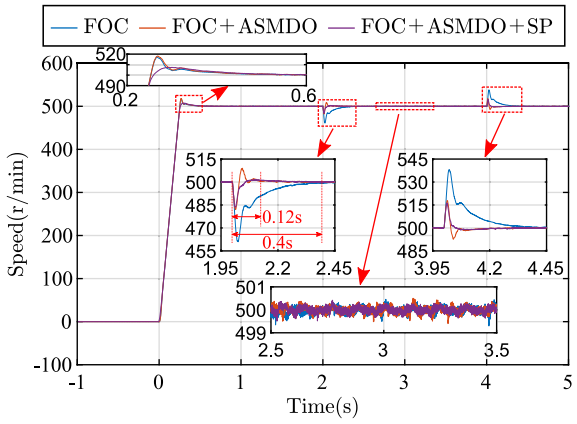

Fig. 15. The speed response at 500 r/min. (Step load disturbance from 0 N·m to rated torque 6 N·m at 2 s and step change from 6 N·m to 0 N·m at 4 s.).

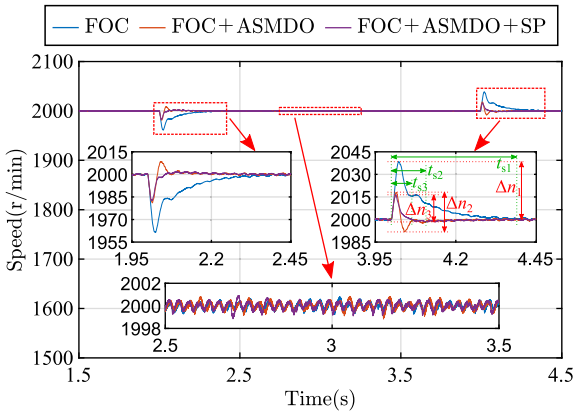

Fig. 16. The speed response at 2000 r/min. (Step load disturbance from 0 N·m to rated torque 6 N·m at 2 s, and step change from 6 N·m to 0 N·m at 4 s.).

"calculated machine torque based on measured current" and "estimated disturbance from ASMDO" as inputs, is adopted to compensate the error caused by the speed filter, so that the undesired speed overshoot/variation can be mitigated. The performance of the proposed solution shown in Fig. 13 is verified by experiments, and the results are presented in detail in the next section.

4. Experimental verification

To demonstrate the effectiveness of the proposed method, experiments based on a PMSM drive system are investigated. The main parameters of the controller and PMSM in the experimental drive system, are given in Table 1 and Table 2 respectively. The experimental platform is shown in Fig. 14. It mainly includes a dSPACE MicroLabBox (DS1202), a test motor, a load machine system, an inverter, and a PC. The switching and sampling frequencies are 5 kHz.

This section is organized as: Section 4.1 demonstrates that the performance of the proposed Smith predictor-assisted adaptive load disturbance rejection controller at different speeds (low, medium, and high speed), and a comparison with the conventional FOC and FOC + ASMDO is included. Section 4.2 shows that the investigation of the calculation burden of the proposed method. Section 4.3 shows the robustness of the proposed method in the presence of moment of inertia mismatch. Section 4.4 demonstrates the generality and effectiveness of the proposed Smith predictor-based speed filter delay compensation structure by collaborating with other disturbance observer, for example, the STSMDO.

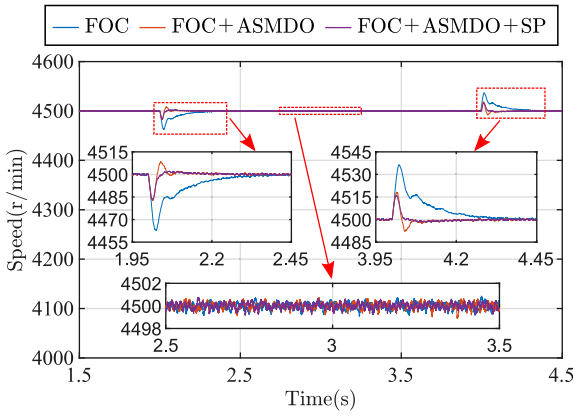

Fig. 17. The speed response at 4500 r/min. (Step load disturbance from 0 N·m to rated torque 6 N·m at 2 s, and step change from 6 N·m to 0 N·m at 4 s.).

4.1. The performance of the proposed disturbance rejection controller under different speeds

To eliminate the speed measurement noise, an LPF with a cut-off frequency of 15 Hz is added to smoothen the speed feedback. The comparison experiments among ASMDO, ASMDO + Smith predictor (SP), with conventional FOC, are carried out at 500 r/min, 2000 r/min, and 4500 r/min respectively. The speed responses when a rated torque step load disturbance (i.e., 6 N·m as listed in Table 2) is applied at time 2 s and removed at 4 s are shown in Fig. 15, Fig. 16, and Fig. 17, respectively.

It can be observed from Fig. 15 that during the start-up phase, there are 3.4 % and 3.6 % overshoot of the speed for FOC and FOC + ASMDO methods, respectively; while for the proposed method, the speed overshoot during the start-up phase is only 1.5 %. In addition, the settling time of these three methods is nearly the same.

When a rated load torque (6 N·m) step change is applied, conventional FOC took 0.4 s to recover from the disturbance. Moreover, speed oscillation can be observed during the transient, which is caused by the speed LPF. However, the duration time of oscillation is less than the speed transient time, i.e., the speed oscillation becomes unobvious after 0.12 s while the speed transient time is about 0.4 s. The oscillation will disappear before the speed returns to its reference value. Therefore, the oscillation can be considered as a secondary factor and does not need extra effort to mitigate it.

While for the control methods with disturbance rejection, the above consideration is no longer suitable. The speed response when ASMDO is implemented for disturbance rejection is illustrated by the dark red curve in Fig. 15. It can be seen that the speed settling time is reduced to about 0.1 s, which is approximately the same with the oscillation time of the FOC control without disturbance rejection. Thus, the speed oscillation becomes a main factor that limits the speed response performance. Apparent overshoot can be observed, and it should be mitigated to further improve the speed transient performance.

SP-based compensator is then added to handle the undesired speed overshoot/variation, and its performance is illustrated by the purple curve in Fig. 15. It can be seen that the undesired speed overshoot is eliminated, which is as expected. The speed settling time is reduced to about 0.055 s only.

When the rated load torque disturbance is removed, similar results with opposite speed variation (i.e., undershoot rather than overshoot) can be observed. The proposed control scheme, i.e., FOC + ASMDO + SP provides the best performance compared with the other two methods. Moreover, experimental results at 2000 r/min and 4500 r/min (rated speed) are shown in Fig. 16 and Fig. 17 respectively. Based on these results, it can be concluded that the proposed solution can work satisfactorily for the whole speed range.

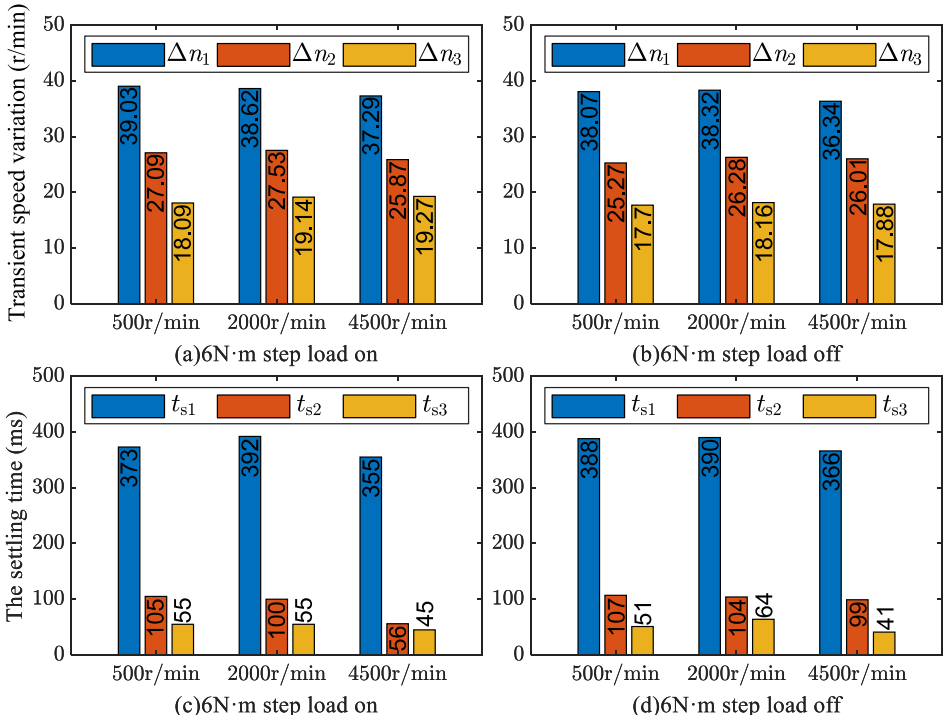

Fig. 18. The transient speed variation and settling time at different working conditions. (Blue bar represents FOC, Dark red bar represents FOC + ASMDO, Yellow bar represents FOC + ASMDO + SP). (For interpretation of the references to colour in this figure legend, the reader is referred to the web version of this article.)

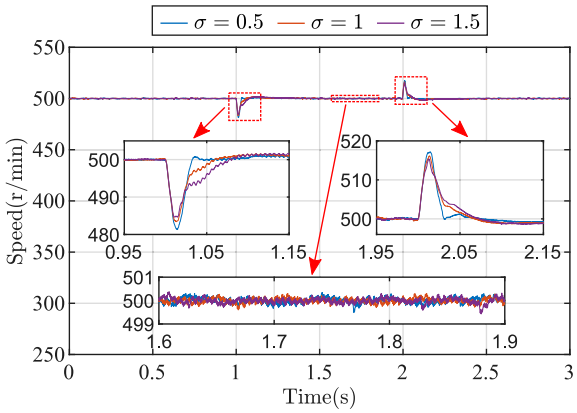

Fig. 19. The speed response at 500r/min with the moment of inertia mismatch.

It is worthwhile to point out that the steady-state speed zoom-in diagrams in Fig. 15, Fig. 16, and Fig. 17 show that the speed steady-state ripples of the three control methods are nearly the same, which means the proposed method will not affect the steady-state performance.

Moreover, to provide a direct comparison among the three methods shown in Figs. 15-17, a histogram is made as shown in Fig. 18, where the "maximum speed variation" and the "settling time" when step load disturbance changes at different speeds are summarized. The definitions of Δn_1, Δn_2, Δn_3, and t_{s1}, t_{s2}, t_{s3} are illustrated in Fig. 16 when taking the step load off as an example. The subscripts 1, 2, and 3 stand for FOC, FOC + ASMDO, and FOC + ASMDO + SP, respectively. It can be observed in Fig. 18 that the transient speed variation and settling time for the same control method are nearly the same for different speeds.

Table 3
Performance of proposed method comparison with parameter mismatch.

Working condition	σ	Maximum transient speed variation	Settling time
Load torque stepping from 0 N·m to 6 N·m	0.5	19.87 r/min	41.8 ms
	1	18.18 r/min	59.8 ms
	1.5	17.08 r/min	77.2 ms
Load torque stepping from 6 N·m to 0 N·m	0.5	18.13 r/min	57.6 ms
	1	17.47 r/min	67.6 ms
	1.5	16.81 r/min	72.6 ms

4.2. The comparison of the calculation burden

To demonstrate the calculation burden of the proposed method, the code execution time of different control methods used in section 4.1 is examined. According to the results, the execution time of FOC + ASMDO only increases by 9.04 % compared to that of FOC, and the execution time of the proposed method (FOC + ASMDO + SP) only increases by 5.5 % compared to that of FOC + ASMDO.

4.3. The effect of moment of inertia mismatch on robustness performance

According to the above analysis in section 3.4, the mismatch of the moment of inertia will not cause the system instability, but it may affect the compensation performance of the proposed method. Additional experiments with moment of inertia mismatch are added. The reference speed is 500 r/min, and the rated step load torque is applied at 1 s and removed at 2 s. The moment of inertia error coefficient σ was set to 0.5, 1, and 1.5 respectively (±50 % mismatch). The experimental results are shown in Fig. 19.

In terms of the steady-state performance of the speed, the zoomed-in plot in Fig. 19 shows that the speed ripples for the three situations are nearly the same. This indicates that the moment of inertia mismatch will not affect the steady-state performance, which is as expected. For the transient performance, the experimental data about the maximum speed

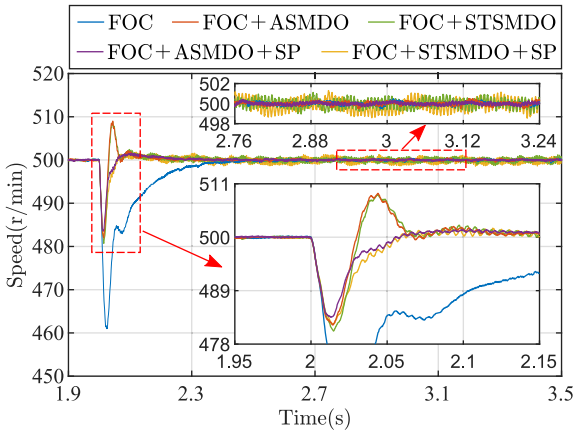

Fig. 20. The speed response of different control schemes.

change in transient and the settling time are summarized in Table 3.

It can be seen that as σ increases, there is a slight decrease in the maximum speed variation during transient response, while the settling time increases. A ± 50 % mismatch of the moment of inertia is considered a relatively large deviation. The mismatch of the moment of inertia does not affect the maximum transient speed variation much, but it does have a slightly greater impact on the settling time. In the worst-case scenario of a step load on transient, the settling time is increased by approximately 30 % as σ increases. However, this performance still outperforms the controller using FOC + ASMDO (without the Smith predictor) with an accurate moment of inertia, which exhibits a maximum speed variation of about 26 r/min and a settling time of approximately 100 ms shown in Fig. 18. Furthermore, as indicated by the analysis in section 3.4, a mismatch of the moment of inertia does not result in any stability issues. Thus, the proposed method has satisfactory robustness against parameter variation.

4.4. The analysis of the Smith predictor versatility

To demonstrate the effectiveness of the Smith predictor under the condition of using different disturbance observers, the ASMDO (ALPF + SMDO) is replaced by STSMDO mentioned in section 2.4. The schemes of FOC + STSMDO and FOC + STSMDO + SP are carried out on the experimental platform and the speed responses are shown in Fig. 20. The rated load torque (6 N·m) step change is applied at time 2 s.

As the experimental results show, during the transient, the green curve (FOC + STSMDO) almost coincides with the dark red curve (FOC + ASMDO), and the yellow waveform (FOC + STSMDO + SP) is also similar to the purple one (FOC + ASMDO + SP). This indicates that when the SP structure is not introduced, the speed overshoot caused by the speed filter is always present, no matter which type of disturbance observer is utilized. However, this problem can be solved satisfactorily by the Smith predictor-based speed filter delay compensator, which can collaborate with different disturbance observers, such as ASMDO and STSMDO.

Furthermore, it has been observed in Fig. 4 that ASMDO demonstrates better performance under steady state condition compared to STSMDO regarding the external disturbance observation – the steady-state ripple of the observed disturbance of ASMDO at loaded condition is smaller than that of STSMDO. Therefore, the speed ripple caused by compensation of the external disturbance observed by ASMDO (purple curve) is smaller than when using STSMDO (yellow curve), as can be observed in Fig. 20.

5. Conclusion

To have a good disturbance rejection ability for servo systems, an improved disturbance rejection controller by utilizing a Smith predictor structure to compensate the error caused by the speed filter is proposed in this paper. The proposed control scheme can eliminate the conjugate poles introduced by the speed filter. Therefore, the problem of oscillatory speed response caused by the speed filter can be mitigated satisfactorily. The experimental results demonstrate that the proposed solution has much better load disturbance rejection performance and good robustness against the parameter mismatch.

CRediT authorship contribution statement

Chao Zhang: Methodology, Software, Validation, Formal analysis, Investigation, Writing – original draft, Data curation, Visualization. **Liwei Zhang:** Resources, Writing – review & editing, Supervision. **Dong Wang:** Conceptualization, Writing – review & editing, Supervision, Project administration. **Kaiyuan Lu:** Investigation, Resources, Writing – review & editing, Supervision.

Declaration of Competing Interest

The authors declare that they have no known competing financial interests or personal relationships that could have appeared to influence the work reported in this paper.

Data availability

Data will be made available on request.

Acknowledgements

This research did not receive any specific grant from funding agencies in the public, commercial, or not-for-profit sectors.

References

[1] Huang S, Wang J, Huang C, Zhou L, Xiong L, Liu J, et al. A fixed-time fractional-order sliding mode control strategy for power quality enhancement of PMSG wind turbine. Int J Electr Power Energy Syst Jan. 2022;134:107354. https://doi.org/10.1016/j.ijepes.2021.107354.

[2] Palanimuthu K, Mayilsamy G, Lee SR, Jung SY, Joo YH. Comparative analysis of maximum power extraction and control methods between PMSG and PMVG-based wind turbine systems. Int J Electr Power Energy Syst Dec. 2022;143:108475. https://doi.org/10.1016/j.ijepes.2022.108475.

[3] Arias A, Ibarra E, Trancho E, Grino R, Kortabarria I, Caum J. Comprehensive high speed automotive SM-PMSM torque control stability analysis including novel control approach. Int J Electr Power Energy Syst Jul. 2019;109:423–33. https://doi.org/10.1016/j.ijepes.2019.02.035.

[4] Benzaouia S, M'Sirdi N, Rabhi A, Naamane A. Integral sliding mode control with exponential reaching law for PMSM in electric vehicles. IFAC-Papers OnLine 2022;55(12):222–7. https://doi.org/10.1016/j.ifacol.2022.07.315.

[5] Asvadi-Kermani O, Felegari B, Momeni H. Adaptive constrained generalized predictive controller for the PMSM speed servo system to reduce the effect of different load torques. e-Prime-Adv Electr Eng Electron Energy 2022;2:100032. https://doi.org/10.1016/j.prime.2022.100032.

[6] Li C, Kang Z. Research on the frequency synchronization control strategy for power system. Int J Electr Power Energy Syst Jan. 2022;134:107407. https://doi.org/10.1016/j.ijepes.2021.107407.

[7] Calasan M, Aleem SHEA, Bulatovic M, Rubezic V, Ali ZM, Micev M. Design of controllers for automatic frequency control of different interconnection structures composing of hybrid generator units using the chaotic optimization approach. Int J Electr Power Energy Syst Jul. 2021;129:106879. https://doi.org/10.1016/j.ijepes.2021.106879.

[8] Yang D, Jin Z, Zheng T, Jin E. An adaptive droop control strategy with smooth rotor speed recovery capability for type III wind turbine generators. Int J Electr Power Energy Syst Feb. 2022;135:107532. https://doi.org/10.1016/j.ijepes.2021.107532.

[9] Ammar A, Kheldoun A, Metidji B, Benakcha M, Bourek A, Benakcha A. Robust model predictive control for induction motor drive using disturbance observer with MRAS speed estimator. Caen, France: ICSC; 2021. p. 516–21. https://doi.org/10.1109/ICSC50472.2021.9666698.

[10] Wang H, Liu L, Fu X. Anti-disturbance control of SPMSM with load torque feedforward compensation. Changchun, China: ICMA; 2018. p. 2306–10. https://doi.org/10.1109/ICMA.2018.8484359.

[11] Ryu SW, Kim J, Rehman AU, Choi HH, Jung JW. A comparative study on reduced-order disturbance observer-based optimal control strategies for surface-mounted

PMSM drives. IEEE Access 2021;9:122983–94. https://doi.org/10.1109/ACCESS.2021.3110259.
[12] Bai C, Yin Z, Zhang Y, Liu J. Robust predictive control for linear permanent magnet synchronous motor drives based on an augmented internal model disturbance observer. IEEE Trans Ind Electron Oct. 2022;69(10):9771–82. https://doi.org/10.1109/TIE.2022.3140532.
[13] Xiao F, Chen Z, Chen Y, Liu H. A finite control set model predictive direct speed controller for PMSM application with improved parameter robustness. Int J Electr Power Energy Syst Dec. 2022;143:108509. https://doi.org/10.1016/j.ijepes.2022.108509.
[14] Lyu M, Wu G, Rao Z, Zheng J, Zhang C, Huang S, et al. Predictive cascaded speed and torque control for A novel three-modular three-phase PMSM. Int J Electr Power Energy Syst Jul. 2021;129:106798. https://doi.org/10.1016/j.ijepes.2021.106798.
[15] Lu W, Zhang Z, Wang D, Lu K, Wu D, Ji K, et al. A new load torque identification sliding mode observer for permanent magnet synchronous machine drive system. IEEE Trans Power Electron Aug. 2019;34(8):7852–62. https://doi.org/10.1109/TPEL.2018.2881217.
[16] Petrella R., Tursini M., Peretti L., Zigliotto M. Speed measurement algorithms for low-resolution incremental encoder equipped drives: a comparative analysis. In: 2007 Int. Aegean Conf. Electr. Mach. Power Electron. Electromotion ACEMP Electromotion Jt. Conf., Bodrum, Turkey 2007;780–787. https://doi.org/10.1109/ACEMP.2007.4510607.
[17] Wang T, Zhu Z, Freire N, Wu Z, Foster M, Stone D. Study on noise and disturbance issues of generalized predictive speed control for permanent magnet synchronous machines. IET Electr Power Appl Jan. 2021;15(1):63–78. https://doi.org/10.1049/elp2.12009.
[18] Wang D, Lu K, Rasmussen PO, Yang Z. Comparative study of low-pass filter and phase-locked loop type speed filters for sensorless control of AC drives. CES Trans. Electr. Mach. Syst. 2015;1(2):207–15 https://doi.org/10.23919/TEMS.2017.7961343.
[19] Zhang Q, Guo H, Guo C, Liu Y, Wang D, Lu K, et al. An adaptive proportional-integral-resonant controller for speed ripple suppression of PMSM drive due to current measurement error. Int J Electr Power Energy Syst Jul. 2021;129:106866. https://doi.org/10.1016/j.ijepes.2021.106866.
[20] Zuo Y, Mei J, Jiang C, Yuan X, Xie S, Lee CHT. Linear active disturbance rejection controllers for PMSM speed regulation system considering the speed filter. IEEE Trans Power Electron Dec. 2021;36(12):14579–92. https://doi.org/10.1109/TPEL.2021.3098723.
[21] Zhang X, Li Z. Sliding-mode observer-based mechanical parameter estimation for permanent magnet synchronous motor. IEEE Trans Power Electron Aug. 2016;31(8):5732–45. https://doi.org/10.1109/TPEL.2015.2495183.
[22] Yang Z, Wang K, Sun X, Ye X. Load Disturbance rejection control of a bearingless induction motor based on fractional-order integral sliding mode. Proc Inst Mech Eng Part I J Syst Control Eng 2018;232(10):1356–64. https://doi.org/10.1177/0959651818782277.
[23] Kim HW, Kim HJ, Choi JY. Multiparameter identification for SPMSMs using NLMS adaptive filters and extended sliding-mode observer. IET Electr Power Appl Apr. 2020;14(4):533–43. https://doi.org/10.1049/iet-epa.2019.0643.
[24] Lian C, Xiao F, Gao S, Liu J. Load torque and moment of inertia identification for permanent magnet synchronous motor drives based on sliding mode observer. IEEE Trans Power Electron Jun. 2019;34(6):5675–83. https://doi.org/10.1109/TPEL.2018.2870078.
[25] Wang B, Luo C, Yu Y, Wang G, Xu D. Antidisturbance speed control for induction machine drives using high-order fast terminal sliding-mode load torque observer. IEEE Trans Power Electron Sept. 2018;33(9):7927–37. https://doi.org/10.1109/TPEL.2017.2765522.
[26] Smith JM. Closer control of loops with dead time. Chem Eng Process 1957;53(5):217–9.
[27] Nie Y, Zhang P, Cai G, Zhao Y, Xu M. Unified smith predictor compensation and optimal damping control for time-delay power system. Int J Electr Power Energy Syst 2020;117:105670. https://doi.org/10.1016/j.ijepes.2019.105670.
[28] Wang Z, Pan K, Xu W. Critical cyber parameters in hybrid power systems with VSP-based virtual inertia emulation: Theoretical approach and mitigation strategy. Int J Electr Power Energy Syst 2023;147:108877. https://doi.org/10.1016/j.ijepes.2022.108877.
[29] Mohamed YARI. Adaptive self-tuning speed control for permanent-magnet synchronous motor drive with dead time. IEEE Trans Energy Convers Dec. 2006;21(4):855–62. https://doi.org/10.1109/TEC.2005.853739.
[30] Wei Y, Wei Y, Sun Y, Qi H, Guo X, Li M. A smith structure-based delay compensation method for model predictive current control of PMSM system. IEEE J Emerg Sel Top Power Electron Aug. 2022;10(4):4090–101. https://doi.org/10.1109/JESTPE.2021.3137299.
[31] Diab AM, Yeoh SS, Bozhko S, Gerada C, Galea M. Enhanced active disturbance rejection current controller for permanent magnet synchronous machines operated at low sampling time ratio. IEEE J Emerg Sel Top Ind Electron April 2022;3(2):230–41. https://doi.org/10.1109/JESTIE.2021.3063919.
[32] Gong C, Hu Y, Ni K, Liu J, Gao J. SM load torque observer-based FCS-MPDSC with single prediction horizon for high dynamics of surface-mounted PMSM. IEEE Trans Power Electron 2020;35(1):20–4. https://doi.org/10.1109/TPEL.2019.2929714.
[33] Xu B, Zhang L, Ji W. Improved non-singular fast terminal sliding mode control with disturbance observer for PMSM drives. IEEE Trans Transp Electrif Dec. 2021;7(4):2753–62. https://doi.org/10.1109/TTE.2021.3083925.
[34] Xu W, Qu S, Zhao L, Zhang H. An improved adaptive sliding mode observer for middle- and high-speed rotor tracking. IEEE Trans Power Electron Jan. 2021;36(1):1043–53. https://doi.org/10.1109/TPEL.2020.3000785.
[35] Qu S, Xu W, Zhao J, Zhang H. Design and implementation of a fast sliding-mode speed controller with disturbance compensation for SPMSM system. IEEE Trans Transp Electrif Dec. 2021;7(4):2611–22. https://doi.org/10.1109/TTE.2021.3060102.
[36] Kim SH. Electric motor control: DC, AC, and BLDC motors. Elsevier; 2017.
[37] Yang C, Song B, Xie Y, Zheng S, Tang X. Adaptive identification of nonlinear friction and load torque for PMSM drives via a parallel-observer-based network with model compensation. IEEE Trans Power Electron 2023;38(5):5875–97. https://doi.org/10.1109/TPEL.2023.3239609.
[38] Jiang J., Wang M., Tang Y., Zhong C., Li L. Super twisting-based position control of PMLSM with load force observer. In: 2019 Int Conf Electr Mach Syst ICEMS, Harbin, China; 2019. p. 1–4. https://doi.org/10.1109/ICEMS.2019.8922258.
[39] Zhou X, Liu M, Ma Y, Wen S. Improved linear active disturbance rejection controller control considering bus voltage filtering in permanent magnet synchronous generator. IEEE Access 2020;8:19982–96. https://doi.org/10.1109/ACCESS.2020.2967395.